RSC Advances

PAPER

View Article Online
View Journal | View Issue

Cite this: *RSC Adv.*, 2026, **16**, 13529

Efficient water electrolysis with Ce-WO_3@NiCo bifunctional catalysts

Yuan Qin, Meng Ding, * Weixiao Ji, Yafang Zhang and Gang Zhao

The development of highly efficient non-precious metal electrocatalysts with excellent activity and durability for overall water splitting remains a critical challenge for advancing sustainable hydrogen production. In this work, Ce-WO_3@NiCo nanoflower architectures are achieved on copper foam (CF) substrates through hydrothermal and electrodeposition methods. Ce doping can improve the activity of catalysts due to the adjustment of the electronic structure, thereby increasing the conductivity. In addition, an electrocatalyst with a three-dimensional (3D) heterostructure can increase the number of active sites, and this multi-component synergistic effect optimizes the electronic structure while regulating the adsorption/desorption process of electrochemical intermediates through interface engineering. The Ce-WO_3@NiCo catalyst exhibits excellent electrocatalytic activity in the alkaline electrolyte, with overpotentials of 56 mV and 323 mV for the hydrogen evolution reaction (HER) and oxygen evolution reaction (OER) respectively, at a current density of 10 mA cm^{-2}. In addition, Ce-WO_3@NiCo requires only 1.624 V to achieve overall water splitting at 10 mA cm^{-2}. Meanwhile, it maintains long-term stability for 72 h at current densities of 10, 100, and 300 mA cm^{-2}. This research offers a viable approach for constructing highly stable and low-cost self-supported bifunctional electrocatalysts through electronic structure modulation.

Received 16th December 2025
Accepted 23rd February 2026

DOI: 10.1039/d5ra09712f

rsc.li/rsc-advances

1. Introduction

The accelerated depletion of fossil fuel reserves and deterioration of environmental problems have made the development of sustainable and high-efficiency renewable energy urgent.[1] Hydrogen (H_2) has emerged as a sustainable energy carrier owing to its conspicuous energy density and negligible CO_2 emission, and is considered as an important force for driving the clean energy transition and achieving carbon neutrality.[2–5] Among various production processes for hydrogen energy, electrocatalytic water decomposition, which involves the hydrogen evolution reaction and oxygen evolution reaction, has been widely recognized as a highly promising method due to its capacity to produce high purity hydrogen without carbon dioxide emissions.[6–10] A selection of electrolytes is crucial in the water electrolysis process, and alkaline electrolytes have received significant attention. In alkaline electrolytes, various catalysts exhibit good stability and high electrolysis efficiency, and the alkaline electrolyte causes minimal corrosion of the equipment.[11,12] Unfortunately, HER kinetics in alkaline electrolytes are two or three orders of magnitude slower than those in acidic conditions, originating from the sluggish water dissociation step and the competitive adsorption of OH^- on catalyst active sites in alkaline systems. The relatively low catalytic efficiency hinders the practical application of the alkaline HER in industrial-scale hydrogen production.[13] Therefore, the development of low-cost, highly active bifunctional HER/OER electrocatalysts in alkaline conditions holds critical importance for enabling energy-efficient pathways toward high-purity hydrogen production.[14]

Recently, transition metal oxides (TMOs) such as WO_3 have attracted increasing attention as bifunctional electrocatalysts for HER and OER, attributed to their natural abundance, cost-effectiveness, and competitive catalytic efficiencies.[15,16] However, the inherently low charge transfer efficiency and sparse catalytic active sites in pure WO_3 limit the further improvement of its water electrolytic performance. Several strategies, such as morphology controlling,[17] phase transition,[18] doping,[19,20] interfacial engineering[21–23] and the microenvironment effect,[24] have been demonstrated to optimize electrocatalytic activity of WO_3. Notably, doping can effectively adjust the electronic structure, reduce the reaction energy barriers for both the HER and OER, thereby significantly enhancing the catalytic activity.[20] For instance, Liang *et al.*[25] prepared Ni-doped tungsten oxide nanorods (Ni-WO_x) for HER in alkaline water and seawater, achieving only 40.51 and 137.04 mV at 10 and 100 mA cm^{-2}, respectively. Furthermore, the Ni-WO_x required 45.69 mV at 10 mA cm^{-2} and had superior stability over 120 h in alkaline seawater. Liu *et al.* reported that the Co-doped WO_3 exhibited a HER overpotential of 117 mV at a current density of 10 mA cm^{-2}.[7] Compared with 3d transition metals (TMs), the Ce

School of Physics and Technology, University of Jinan, 336 West Road of Nan Xinzhuang, Jinan, 250022, People's Republic of China. E-mail: sps_dingm@ujn.edu.cn

element with 4f electrons exhibits oxidation states of +3 and +4, enabling redox interaction between Ce^{3+} and Ce^{4+},[26] thus it has a relatively prominent advantage in the field of electrocatalysis.

TMs alloys, especially Ni and Co, remain a research focus owing to their structurally adaptive coordination environments and versatile reactivity in multi-step catalytic cycles. These properties, including mechanical strength, magnetism and catalytic activity, are closely related to their tunable d-orbital configurations and chemical structures.[9,27,28] TM-based catalysts have been demonstrated exceptional ability in promoting HO–H bond dissociation. Coupled interfacial effects emerge when combined with other electrocatalytic materials, which significantly enhance the reaction dynamics of alkaline water splitting processes.[29–31] However, the intrinsically sluggish water dissociation kinetics of such composite systems fundamentally constrain their catalytic efficiency under alkaline conditions.[32] Heterostructures[33,34] are widely constructed to improve their electrocatalytic performance by enhancing interfacial electron transfer kinetics, and concurrently optimizing reactant adsorption energetics and charge transport capabilities.[5,35,36] Li *et al.* reported that $NiCoO_2$/NiCo@C, synthesized *via* a two-step method, exhibits HER and OER overpotentials of only 61.9 and 329 mV at 10 mA cm^{-2}.[37] Therefore, NiCo alloy can be used to construct heterostructures with other oxides to enhance the overall water splitting performance.[38]

In this work, Ce-WO_3@NiCo heterostructures were synthesized by hydrothermal and electrodeposition method, and served as a bifunctional electrocatalyst to evaluate overall water splitting performance. The integration of Ce-WO_3 and NiCo establishes robust interfacial coupling effects that significantly accelerate charge transfer kinetics and improve conductivity, collectively contributing to the electrocatalytic performance. The Ce-WO_3@NiCo catalyst exhibited excellent electrochemical activity for both the HER and OER. The use of Ce-WO_3@NiCo as both cathode and anode enabled systematic evaluation of the full water electrolysis process.

2. Experimental methods

2.1. Materials

Copper foam (1 × 1 cm^2) was served as the substrate. Reagents including absolute ethanol (CH_3CH_2OH, ≥99.7%) and potassium hydroxide (KOH, ≥85%), also metal chloride precursors: nickel(II) chloride hexahydrate ($NiCl_2 \cdot 6H_2O$, ≥98.0%), cobalt(II) chloride hexahydrate ($CoCl_2 \cdot 6H_2O$, ≥99.0%), cerium(III) chloride heptahydrate ($CeCl_3 \cdot 7H_2O$, ≥99.0%), and tungsten(VI) chloride (WCl_6, ≥99.9%)are of analytical grade and supplied by Sinopharm Chemical Reagent Co., Ltd.

2.2. Synthesis of Ce-WO_3

The Ce-WO_3 nanostructures were synthesized *via* the hydrothermal method on copper foam (CF) substrates. First, several pieces of CF (1 × 1 cm^2) were sequentially ultrasonic cleaned in 3 M HCl, absolute ethanol, and deionized water (resistivity: 18.2 MΩ cm). Subsequently, a precursor solution was obtained through dissolution of 250 mg WCl_6 and 0.0468 g $CeCl_3 \cdot 7H_2O$ in 40 mL absolute ethanol, and magnetic stirring over 30 minutes. The obtained solution was transferred into an 80 mL Teflon-lined stainless steel autoclave, and the cleaned CF pieces were immersed for the subsequent reaction. The autoclave underwent thermal processing at 180 °C for 12 h in a controlled oven environment, followed by spontaneous cooling to ambient temperature. The obtained Ce-WO_3/CF was sequentially rinsed with absolute ethanol and deionized water to remove inorganic and organic residues. And finally, the resultant material was vacuum-dried at 60 °C for 6 hours. For comparative analysis, pure WO_3 nanostructure were fabricated *via* identical synthesis method without $CeCl_3 \cdot 7H_2O$.

2.3. Synthesis of Ce-WO_3@NiCo

NiCo was synthesized on Ce-WO_3 *via* electrochemical deposition using a three-electrode configuration. The Pt sheet, Ag/AgCl (3.5 M Cl^-) and *in situ* growth of Ce-WO_3 on CF were used as counter, reference and working electrode, respectively. Electrodeposition was conducted at a constant potential of −1.0 V (*vs.* Ag/AgCl) for 20 minutes using an electrochemical workstation in a solution composed of 0.1 M KCl, 0.05 M $NiCl_2 \cdot 6H_2O$, and 0.02 M $CoCl_2 \cdot 6H_2O$ under ambient temperature conditions.[39]

2.4. Characterization

The morphology and elemental mapping were characterized by field-emission scanning electron microscopy (FE-SEM, FEI Quanta FEG 250). The crystal structure of electrocatalysts was characterized by X-ray diffraction (XRD, Rigaku Ultima IV, Cu Kα $\lambda = 1.5406$ Å). The surface valence states of electrocatalysts were analyzed by X-ray photoelectron spectroscopy (XPS, Thermo Scientific K-Alpha) with Al Kα radiation, calibrated using the adventitious carbon peak (C 1s at 284.8 eV). The lattice structure and morphology were resolved by high-resolution TEM imaging employing an FEI Talos F200X microscope.

2.5. Electrochemical measurements

Electrochemical measurements of as-prepared electrocatalysts were conducted using a CHI 760E workstation with a standard three-electrode system: Ag/AgCl (reference electrode), Pt foil (counter electrode), and catalyst-coated substrate (working electrode) in 1.0 M KOH electrolyte. Linear sweep voltammetry (LSV) analysis of the catalysts was conducted at scan rate of 5 mV s^{-1}. The experimental data were normalized to the reversible hydrogen electrode (RHE) through the Nernst equation: E (*vs.* RHE) = E (*vs.* Ag/AgCl) + 0.197V + 0.05916 × pH. The double layer capacitance (C_{dl}) of different catalysts was measured using cyclic voltammetry (CV) with the voltage *vs.* RHE ranging from 0 to 0.1 V, and the CV curves were obtained at sweep rates spanning from 20 to 100 mV s^{-1} with a stepwise increment of 20 mV s^{-1}. The electrochemical impedance spectroscopy (EIS) was studied with the frequency ranging from 1 × 10^5 to 1 × 10^{-2} Hz. Stability was evaluated by chronoamperometry at current densities of 10, 100, and 300 mV s^{-1}, respectively. All the electrochemical measurements were performed at room temperature.

3. Results and discussion

Fig. 1(a) illustrates the two-step synthetic process of the Ce-WO_3@NiCo electrocatalyst. Copper foam was selected as the growth substrate for its good conductivity, three dimensional multi-porous structure and structural stability. First, the Ce-WO_3 nanosheets were synthesized *via* hydrothermal method with different Ce doping concentrations. Subsequently, the NiCo layer was deposited onto the surface of Ce-WO_3 nanosheets *via* electrochemical deposition. Finally, the flower-like three-dimensional Ce-WO_3@NiCo heterostructure was formed on CF substrate.

The morphological features of as-synthesized WO_3, NiCo, Ce-WO_3, and Ce-WO_3@NiCo were analyzed *via* SEM. As was revealed in Fig. 1(b), the pure WO_3 catalyst displayed an interconnected nanosheet architecture. The pure NiCo alloy layer

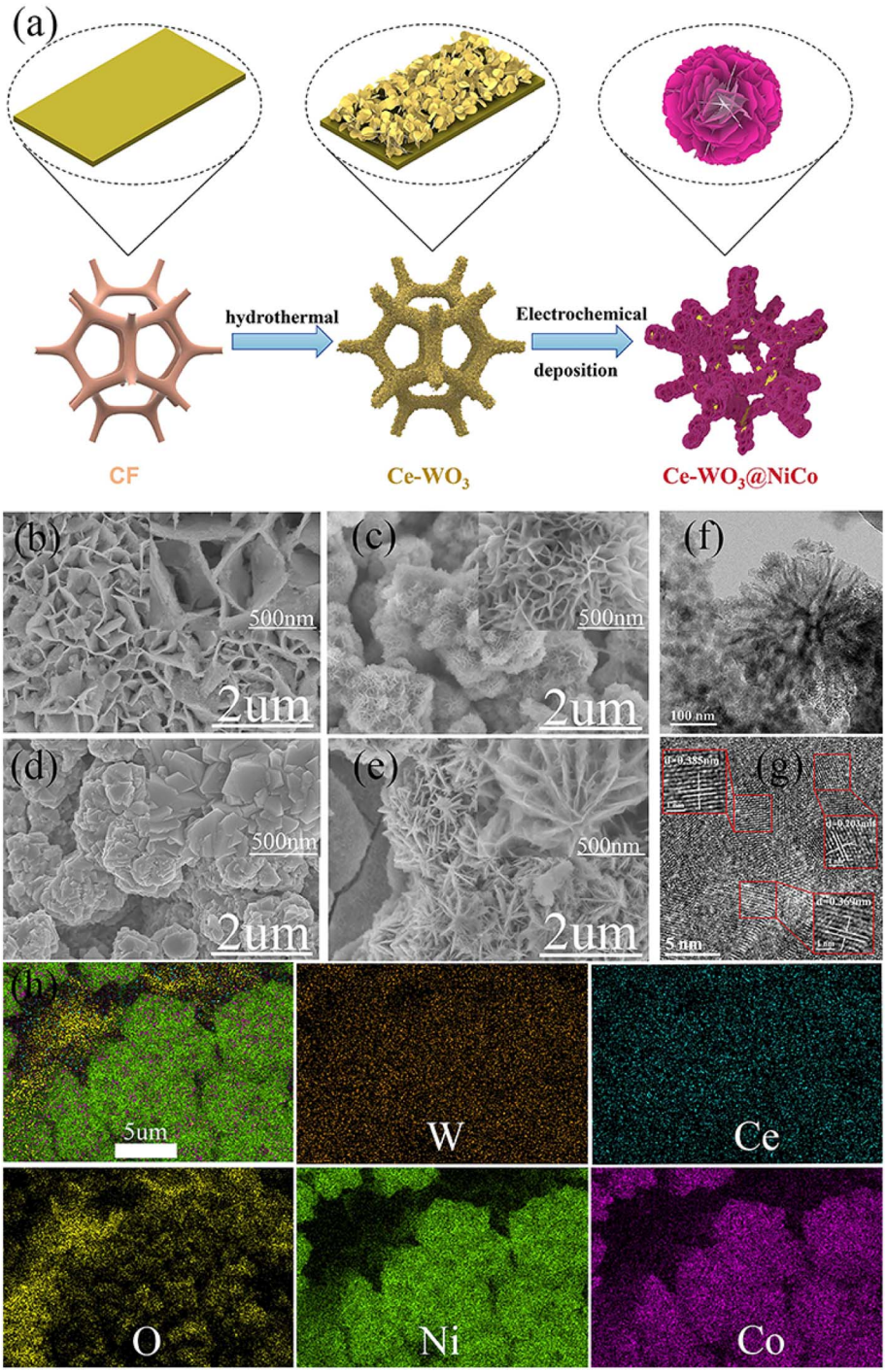

Fig. 1 (a) Synthesis process of Ce-WO_3@NiCo. SEM images of (b) WO_3, (c) NiCo, (d) Ce-WO_3, (e) Ce-WO_3@NiCo, (f) TEM, (g) HRTEM images of Ce-WO_3@NiCo, (h) SEM image of Ce-WO_3@NiCo, and the associated energy-dispersive spectroscopy (EDS) elemental mapping of W, Ce, O, Ni, and Co.

was sphere-like structure formed by the interweaving and stacking of nanosheets on the CF substrate, which was conducive to exposing active sites (Fig. 1(c)). For Ce-WO_3, the doping of Ce significantly elevated the formation energy of oxygen vacancy (Fig. 1(d)),[40] thereby suppressing the dissolution of tungsten under alkaline conditions and enhancing its structural stability. Meanwhile, heteroatom doping introduces ionic mismatch, leading to lattice distortion[41] and internal strain.[42] To alleviate this strain, the nanosheets fragment and trigger recrystallization. Furthermore, the distorted lattice disrupts the original growth anisotropy, suppressing the expansion of the initially preferred planes while enhancing growth in perpendicular directions. Consequently, the doping could increase the thickness of the nanosheets and form denser particles. As illustrated in Fig. 1(e), the Ce-WO_3@NiCo composite exhibited a three-dimensional nanoflower architecture composed of tightly interconnected ultrathin nanosheets. This unique structure not only provides additional active edge sites but also increases the specific surface area, reduces the charge transfer distance between active species, and thereby enhances overall conductivity. The microstructure of Ce-WO_3@NiCo was further characterized by TEM and HRTEM. The TEM image confirmed the presence of the nanoflower structure, which was consistent with the SEM result. HRTEM analysis (Fig. 1(g)) revealed lattice spacings of 0.203, 0.385, and 0.369 nm, corresponding to the NiCo (111) and WO_3 (001)/(200) lattice planes, respectively. The EDS elemental mapping images (Fig. 1(h)) confirmed the uniform distribution of O, Co, Ni, Ce, and W elements in the Ce-WO_3@NiCo catalyst. In summary, the TEM results further verified the successful fabrication of the Ce-WO_3@NiCo heterostructure.

The crystallographic structure of the samples was characterized using X-ray diffraction. Fig. 2(a) displayed the XRD patterns of as-synthesized samples, and the XRD patterns of undoped WO_3 and Ce-doped WO_3 with varying Ce contents were plotted in Fig. S1. The XRD patterns were dependent on the Ce concentration. For Ce-doped WO_3, the introduction of Ce could reduce the diffraction peak intensity of WO_3 compared to the undoped, probably resulting from lattice compression and poor crystallinity induced by Ce dopants.[43] Furthermore, the diffraction peak of CeO_2 would appear when the doping concentration of Ce reached a certain extent, which may affect the properties of the WO_3.[43] The XRD result also showed that WO_3 has been synthesized by the hydrothermal method, and 2θ = 23.083, 23.707, 24.098, 28.775, and 34.022 corresponded to (002), (020), (200), (111), and (220) crystal planes, respectively, which matched the pattern of WO_3 (#00-020-1324). The peaks at $2\theta = 44.428°$, 51.768°and 76.25°, corresponding to (111), (200) and (220) crystal planes, matched the pattern of NiCo alloy (#00-003-2246). And three distinct peaks at $2\theta = 43.407°$, 50.556° and 74.297°, corresponding to the (111), (200), and (220) planes of CF(#00-004-0836) were observed.

The surface elemental composition and chemical states were analyzed using X-ray photoelectron spectroscopy. The W 4f spectra of different samples were shown in Fig. 2(b). Two peaks observed at 35.47 eV and 37.69 eV in the W 4f spectrum of WO_3 was assigned to the W $4f_{7/2}$ and W $4f_{5/2}$ orbitals. The binding energy of W $4f_{7/2}$ in Ce-WO_3 was offset by about 0.1 eV, higher than pure WO_3, and the higher binding energy shift indicated electron transfer from W to Ce.[44] The W 4f XPS spectrum of Ce-WO_3@NiCo exhibited two peaks at 35.02 eV (W $4f_{7/2}$) and 37.19 eV (W $4f_{5/2}$). The W $4f_{7/2}$ binding energy of Ce-WO_3@NiCo was negatively shifted by about 0.55 eV compared to the W $4f_{7/2}$ binding energy of Ce-WO_3.[7,45] These results showed that Ce-WO_3@NiCo had electron transfer and interface coupling interaction between Ce-WO_3 and NiCo heterogeneous interfaces. In the Ni 2p XPS spectrum of Ce-WO_3@NiCo (Fig. 2(c)), it could be seen that two spin–orbit coupling peaks at binding energies of 855.6 eV and 873.3 eV, corresponding to Ni^{2+}. Furthermore, the satellite peaks located at 861.3 eV ($2p_{3/2}$) and 877.6 eV ($2p_{1/2}$), and the Ni^0 peak at 852.1 eV were observed.[46,47] For the Co 2p XPS curve of Ce-WO_3@NiCo (Fig. 2(d)), the peaks at 781.8 eV ($2p_{3/2}$) and 796.7 eV ($2p_{1/2}$) indicated the presence of surface oxidation states, and the other two lower peaks at 786.2 eV and 803.4 eV were attributed to the satellite peaks. Moreover, the peak located at 777.7 eV was assigned to Co^0.[46,48,49] The high-resolution spectrum of Ce 3d (Fig. 2(e)) revealed characteristic spin–orbit doublets, with the binding energy range of 895.5–904.9 eV corresponding to Ce $3d_{3/2}$ states and 881.7–882.4 eV associated with Ce $3d_{5/2}$. The peaks of Ce^{3+} located at 881.7 and 900.1 eV, and the five peaks of Ce^{4+} at 882.4, 895.5, 899.5, 902.7, and 904.9 eV, clearly indicated the existence of both trivalent and tetravalent cerium ions in the sample.[35,43] The O 1s in Fig. 2(f) was split into three distinct peaks at 529.96 eV, 531.32 eV, and 532.53 eV, attributed to metal–oxygen bonds, hydroxyl groups, and adsorbed water molecules, respectively. Notably, the binding energy of the O 1s orbital exhibited a 0.55 eV positive shift compared with pristine WO_3.[44,50,51] These experimental results showed that the coupling between Ce-WO_3 and NiCo could form a heterogeneous interface with strong electronic interaction.

Comparative HER studies were carried out in 1.0 M KOH employing a tri-electrode potentiostat setup. First, the effect of heteroatom doping on the catalytic performance of the material was investigated; and the HER performance of Ce-WO_3 with varying amounts of Ce was studied (Fig. S2). It can be observed that the Ce doping significantly enhanced HER performance, which could be attributed to the Ce-induced charge transfer that modified the intrinsic electronic structure of WO_3. Polarization curve analysis in Fig. 3(a) revealed the superior catalytic property of Ce-WO_3@NiCo under various potentials compared with CF, NiCo, WO_3, and Ce-WO_3. The Ce-WO_3@NiCo achieved a low HER overpotential (η) of 56 mV at 10 mA cm^{-2}, showing much lower overpotentials than that of CF (262 mV), NiCo (135 mV), WO_3 (211 mV), and Ce-WO_3 (170 mV) at the same current density. Additionally, the overpotential required by Ce-WO_3@-NiCo was slightly higher than that of Pt/C (Fig. S3), and it exhibited superior electrocatalytic performance compared to the reported other electrocatalysts (as shown in Table S1). The Tafel slopes derived from the LSV curves of these electrocatalysts were shown in Fig. 3(b). In the range of 1.1–2.0 V, the Tafel slopes for CF, NiCo, WO_3, Ce-WO_3, and Ce-WO_3@NiCo were 280.77, 129.71, 268.66, 146.09, and 128.21 mV dec^{-1}, respectively. A comparison between WO_3 and Ce-WO_3

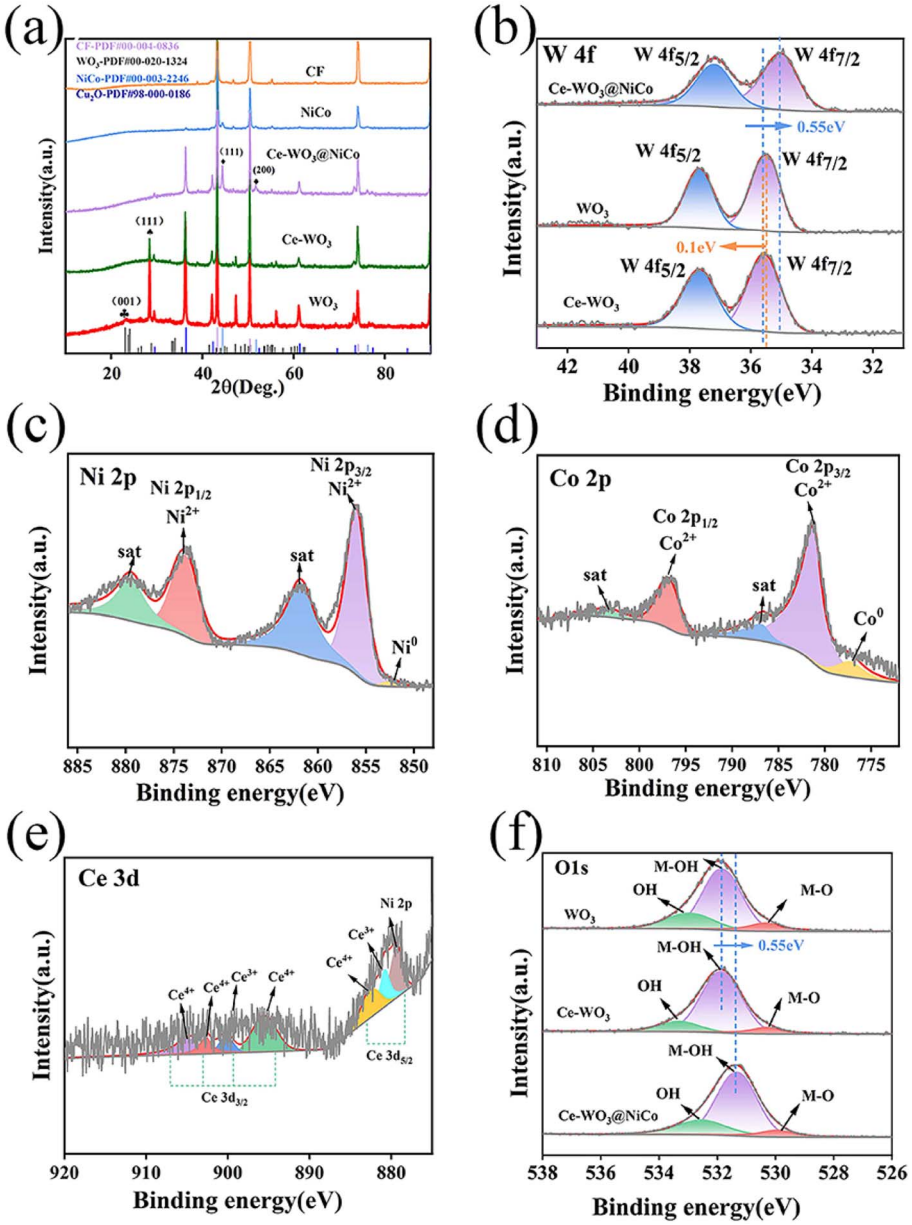

Fig. 2 (a) XRD patterns of Ce-WO_3@NiCo, NiCo, Ce-WO_3, WO_3, and CF. XPS elemental spectra of different samples: (b) W 4f, (c) Ni 2p, (d) Co 2p, (e) Ce 3d, (f) O 1s.

demonstrated that Ce doping accelerated the HER reaction kinetics. The lower Tafel slope of Ce-WO_3@NiCo indicated that the interfacial coupling between Ce-WO_3 and NiCo could promote water dissociation and hydrogen adsorption. To elucidate HER activity enhancement mechanisms, the electrochemically active surface area (ECSA) of electrocatalysts was systematically characterized. The CV scans in the non-Faradaic potential region were performed at different scan rates (Fig. S4), and the double-layer capacitance (C_{dl}), which was linearly related to ECSA, was obtained by fitting the CV curves. Fig. 3(c) revealed that the C_{dl} of CF, WO_3, Ce-WO_3, NiCo, and Ce-WO_3@NiCo were 9.46, 11.2, 15.26, 16.21, and 35.34 mF cm^{-2}, respectively. From the experimental results, Ce-WO_3@NiCo was demonstrated a significantly enhanced electrochemically active surface area and more exposed active sites compared to other electrocatalysts. It was likely attributed to its rougher surface morphology that led to enhanced hydrophilicity, which further confirmed the structure–activity correlation.[52] Normalization of LSV curves was performed *via* ESCA, with the normalized data presented in Fig. S5. It could be observed from the figure that Ce-WO_3@NiCo still exhibited excellent performance in the normalized LSV curves. The EIS measurements were performed to investigate interfacial charge transfer behavior across electrode/electrolyte interfaces, and the interfacial kinetics during the HER process were revealed. The Nyquist curves of CF, WO_3, Ce-WO_3, NiCo, and Ce-WO_3@NiCo were presented in

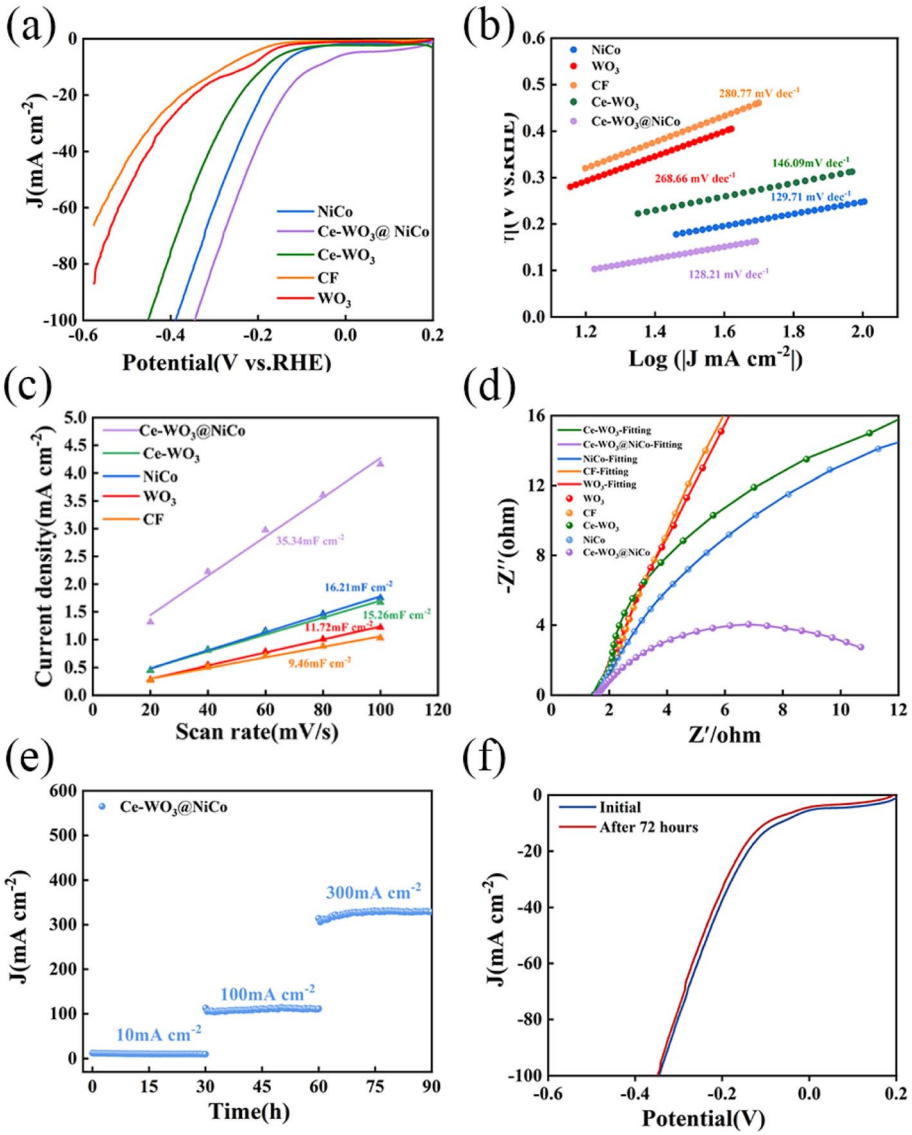

Fig. 3 HER performance of CF, NiCo/CF, WO_3/CF, Ce-WO_3, and Ce-WO_3@NiCo samples: (a) LSV curves, (b) Tafel slopes, (c) C_{dl} measurement, (d) EIS plots, (e) stability test at different current densities, (f) LSV curves before and after Ce-WO_3@NiCo stability test.

Fig. 3(d). The equivalent circuit diagram and the fitting results of experimental data are depicted in Fig. S6 and Table S2, respectively. The equivalent circuit employed for fitting was consisted of one series resistance (R_s) and two parallel combinations of charge transfer resistance (R_{ct}) and constant phase element (CPE). It could be observed from the Nyquist plot in Fig. 3(d) that Ce-WO_3@NiCo exhibited the smallest semicircle diameter, indicating the lowest charge transfer resistance. The specific values are provided in Table S3, which demonstrated that Ce-WO_3@NiCo possessed the fastest charge transfer kinetics. The Ce-WO_3@NiCo heterostructure could improve charge transfer ability and increase the electron migration rate, thereby enhancing HER performance.[53–56] In addition to the excellent HER activity, the stability of HER was also investigated. The durability test of Ce-WO_3@NiCo was shown in Fig. 3(e and f), the catalytic stability was evaluated at 10, 100, and 300 mA cm^{-2} through *i–t* tests, and no significant attenuation in the curves was observed. The LSV plots of Ce-WO_3@NiCo before and after the electrochemical test were compared, and the good degree of overlap demonstrated that Ce-WO_3@NiCo possessed outstanding electrochemical stability in HER. As shown in Fig. S7, the multi-step chronopotentiometry measurements were performed on WO_3, Ce-WO_3, NiCo, and Ce-WO_3@NiCo working electrodes across a current density range of 10–210 mA cm^{-2} with a step increment of 40 mA cm^{-2}. Compared with electrocatalysts, Ce-WO_3@NiCo exhibited the lowest initial potential, and this trend and this trend was maintained under different current densities. Specifically, Ce-WO_3@NiCo exhibits excellent catalytic activity, along with satisfactory stability under stepwise increasing current densities. Generally, the outstanding HER activity and stability of Ce-WO_3@NiCo could be attributed to three factors: (1) the direct growth of Ce-WO_3 nanosheets on CF as a scaffold for subsequent NiCo nanosheets deposition

strengthened interfacial connectivity, promoting the rapid charge transfer. (2) The three-dimensional hierarchical structure provided abundant catalytic sites and therefore facilitated gas release and prevented mechanical detachment. (3) The synergistic effect in the Ce-WO_3@NiCo heterostructure enhanced its electrochemical activity.

The OER catalytic performance of as-synthesized samples was comprehensively compared under standardized testing conditions. To achieve superior electrochemical activity in Ce-WO_3, the OER performance under different Ce doping levels was studied (Fig. S2). It was observed that Ce-doped WO_3 always exhibited much better OER performance than pure WO_3. An oxidation peak was identified in the forward scanning LSV curve, which prevented the evaluation of η_{10}. To suppress the interference of oxidation peaks, the LSV curves in Fig. 4(a) were recorded in reverse scan mode from high to low potentials. The LSV curves of Ce-WO_3@NiCo showed significantly enhanced reduction peaks, with their integrated peak area being much larger than that of the NiCo alloy. Additionally, the shift of the reduction peak indicated that the Ce-WO_3@NiCo hetero-interface had a higher density of active sites and faster electron migration rates.[57] The enhanced redox dynamics and accelerated electron migration could improve OER reaction kinetics. At a current density of 10 mA cm^{-2}, Ce-WO_3@NiCo exhibited a substantially reduced overpotential (323 mV) compared to CF (391 mV), NiCo (355 mV), WO_3 (388 mV), and Ce-WO_3 (374 mV), and exhibited outstanding OER electrocatalytic activity than most of the catalysts reported in previous work (Table S3). Analysis of the kinetics of the OER was conducted according to the Tafel slopes calculated from LSV polarization curves. In Fig. 4(b), the Tafel slopes of CF, NiCo, WO_3, Ce-WO_3, and Ce-WO_3@NiCo were fitted to be 237, 190, 222, 203, and 175 mV dec^{-1}, respectively. The lowest Tafel slope of Ce-WO_3@NiCo indicated its faster OER reaction kinetics, suggesting that the catalyst possessed rapid electron migration and efficient mass transport. Additionally, the large Tafel slope in this range was likely due to the influence of oxidation peaks of Co/Ni ions during testing. The durability test of Ce-WO_3@NiCo was shown in Fig. 4(c and d), the catalytic stability was evaluated at 10, 100, and 300 mA cm^{-2} through *i–t* tests, and no obvious attenuation in the LSV curves was observed. The LSV curves of Ce-WO_3@NiCo before and after the electrochemical test were compared, and the good degree of overlap demonstrated that Ce-WO_3@NiCo possessed excellent electrochemical stability in OER.

Given the superior catalytic activity of the Ce-WO_3@NiCo heterostructure, an integrated electrolyser was constructed and it served as cathode and anode electrodes for efficient alkaline water splitting. The polarization curves of Ce-WO_3@NiCo//Ce-WO_3@NiCo were investigated in 1 M KOH, as shown in Fig. 5(a). Ce-WO_3@NiCo exhibited a low operating potential of 1.624 V to achieve 10 mA cm^{-2}, showing 6.8–15.6% voltage reduction compared to control groups: CF (2.034 V), NiCo (1.702 V), Ce-WO_3 (1.827 V), and WO_3 (1.840 V). Table S4 presents the overall water splitting performance of Ce-WO_3@NiCo and other reported catalysts at a current density of 10 mA cm^{-2}. Compared with previous catalysts, the Ce-WO_3@NiCo composite operates at

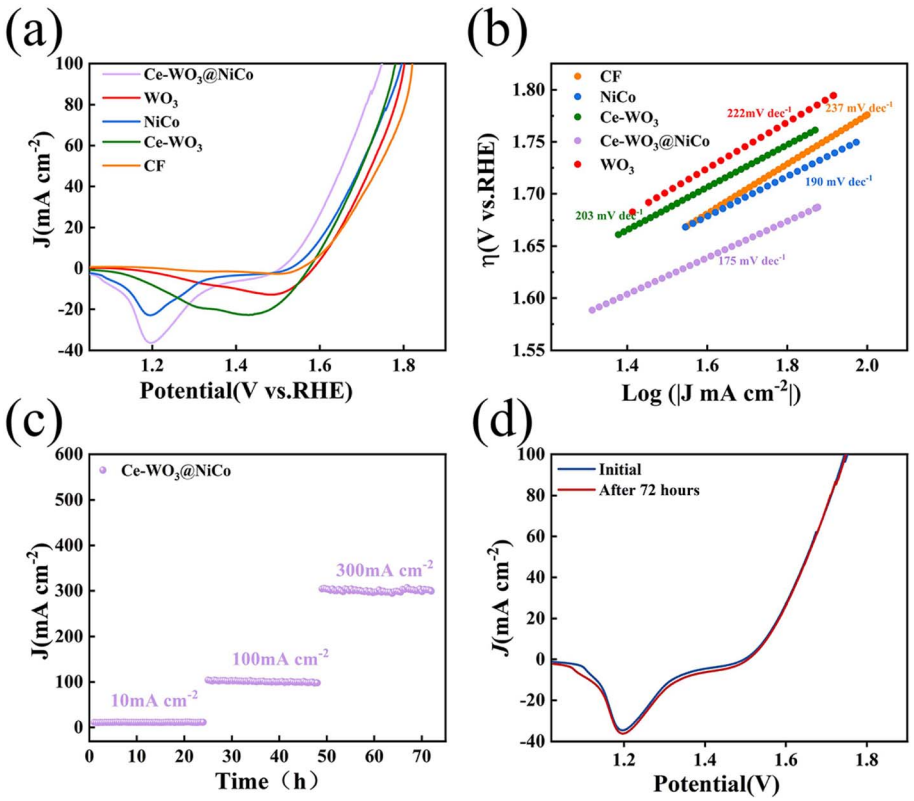

Fig. 4 OER performance of the as-grown samples: (a) LSV curves at scan rate of 5 mV s^{-1}, (b) Tafel slopes, (c) stability test, (d) LSV curves before and after stability test of Ce-WO3@NiCo.

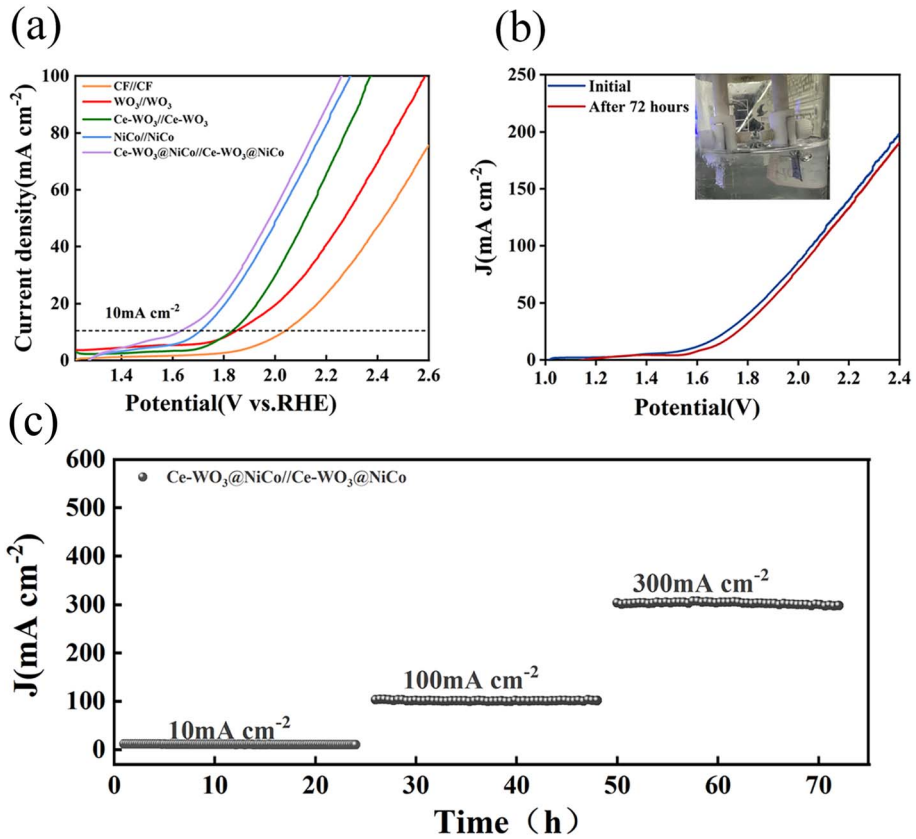

Fig. 5 (a) The overall hydrolysis performance of the sample, (b) electrochemical durability evaluation of Ce-WO_3@NiCo for overall water splitting through comparative pre-/post-stability LSV measurements, (c) stability test over 72 h.

a lower overpotential, indicating excellent catalytic activity for overall water splitting in alkaline electrolytes. Fig. 5(b) revealed minimal divergence between the LSV curves before and after the stability test, confirming superior electrochemical stability. The morphology and crystal structure of the Ce-WO_3@NiCo electrocatalyst after the durability test of 72 h were further studied. XRD and SEM images revealed that the structure was well preserved and that the surface shape of the Ce-WO_3@NiCo material did not change significantly, as shown in Fig. S8 and S9. The Ce-WO_3@NiCo nanostructure exhibited long-lasting catalytic stability (Fig. 5(c)) no noticeable degradation after 72 h undergoing sequential testing at 10, 100, and 300 mA cm^{-2} for 24 h each at room temperature. The Ce-WO_3@NiCo catalyst maintained structural integrity under large current density of 300 mA cm^{-2}. The Ce-WO_3@NiCo was demonstrated exceptional OER/HER bifunctionality and stability, establishing its potential in industrial-scale overall water splitting as an emerging catalyst.

4. Conclusions

In this paper, the Ce-WO_3@NiCo for water splitting in an alkaline environment was prepared using hydrothermal and electrodeposition methods. The Ce-WO_3@NiCo heterostructure had excellent bifunctional electrocatalytic activity and stability due to doping and synergistic effects. The catalyst achieved low overpotentials of 56 mV and 323 mV at 10 mA cm^{-2} for HER and OER, respectively. The superior catalytic performance originated from interfacial charge transfer dynamics and dopant-induced electronic modulation. The Ce-WO_3@NiCo as bifunctional catalyst was used as cathode and anode of an electrolyzer. Notably, the potential of Ce-WO_3@NiCo was only 1.624 V at 10 mA cm^{-2}, also it had superior overall water splitting stability. In this study, a feasible design is established to fabricate an efficient and inexpensive bifunctional catalyst through interface engineering to address key challenges in industrial hydrogen production systems.

Author contributions

Yuan Qin: investigation, writing – original draft. Meng Ding: funding acquisition, writing – review & editing. Weixiao Ji: conceptualization. Yafang Zhang: supervision. Gang Zhao: project administration.

Conflicts of interest

The authors declare that they have no known competing financial interests or personal relationships that could have appeared to influence the work reported in this paper.

Data availability

The data that support the findings of this study are available from the corresponding author upon reasonable request.

Supplementary information (SI) is available. See DOI: https://doi.org/10.1039/d5ra09712f.

Acknowledgements

The work was funded by the project (No. ZR2022MB142) supported by Shandong Provincial Natural Science Foundation.

References

1 B. Liu, R. Li, B. Liu, G. Wang, J. Sun, H. Huang, H. Shi and J. Zhang, Z-scheme WO_3/AgI heterojunction grown on flexible carbon fibres for efficient organic degradation and bacterial inactivation, *J. Water Process Eng.*, 2024, **64**, 105704, DOI: 10.1016/j.jwpe.2024.105704.

2 A. M. R. Ramírez, S. Heidari, A. Vergara, M. V. Aguilera, P. Preuss, M. B. Camarada and A. Fischer, Rhenium-Based Electrocatalysts for Water Splitting, *ACS Mater. Au*, 2023, **3**, 177–200, DOI: 10.1021/acsmaterialsau.2c00077.

3 Q. Huang, Z. Y. Sun and Y.-L. Du, Enhancing safety in hydrogen storage: Understanding the dynamic process in hydrogen-methane mixtures during the pressurized leakage, *Process Saf. Environ. Prot.*, 2024, **192**, 1554–1565, DOI: 10.1016/j.psep.2024.10.100.

4 M. L. Yu, K. Wang and H. Vredenburg, Insights into low-carbon hydrogen production methods: Green, blue and aqua hydrogen, *Int. J. Hydrogen Energy*, 2021, **46**, 21261–21273, DOI: 10.1016/j.ijhydene.2021.04.016.

5 J. Seo, S. Jeon, S. Lee, D.-K. Lim, J. H. Kim, J. H. Kim, S. Ahn and W. Jung, Oxidative Strong Metal-Support Interaction Induced by an Amorphous TiOx Seed Layer Boosts the Electrochemical Performance and High-Temperature Durability of Pt Nanocatalysts, *ACS Catal.*, 2022, **12**, 8593–8600, DOI: 10.1021/acscatal.2c00947.

6 Y. Yan, B. Xia, Z. Xu and X. Wang, Recent Development of Molybdenum Sulfides as Advanced Electrocatalysts for Hydrogen Evolution Reaction, *ACS Catal.*, 2014, **4**, 1693–1705, DOI: 10.1021/cs500070x.

7 L. Liu, Y. Zhao, Y. Wang, Z. Zhang, J. Liu, T. Wu, W. Qin, S. Liu, B. Jia, H. Wu, D. Zhang, X. Qu, K. Xi and M. Qin, Single-Atom Co Doped in Ultrathin WO_3 Arrays for the Enhanced Hydrogen Evolution Reaction in a Wide pH Range, *ACS Appl. Mater. Interfaces*, 2021, **13**, 53915–53924, DOI: 10.1021/acsami.1c16082.

8 J. Chen, D. Yu, W. Liao, M. Zheng, L. Xiao, H. Zhu, M. Zhang, M. Du and J. Yao, WO_{3-x} Nanoplates Grown on Carbon Nanofibers for an Efficient Electrocatalytic Hydrogen Evolution Reaction, *ACS Appl. Mater. Interfaces*, 2016, **8**, 18132–18139, DOI: 10.1016/j.cej.2020.127089.

9 C. Cheng, F. Zheng, C. Zhang, C. Du, Z. Fang, Z. Zhang and W. Chen, High-efficiency bifunctional electrocatalyst based on 3D freestanding Cu foam in situ armored CoNi alloy nanosheet arrays for overall water splitting, *J. Power Sources*, 2019, **427**, 184–193, DOI: 10.1016/j.jpowsour.2019.04.071.

10 J. J. Li, S. B. Zou, X. D. Liu, Y. Lu and D. H. Dong, Electronically Modulated CoP by Ce Doping as a Highly Efficient Electrocatalyst for Water Splitting, *ACS Sustainable Chem. Eng.*, 2020, **8**, 10009–10016, DOI: 10.1021/acssuschemeng.0c01193.

11 Y. Y. Ning, D. D. Ma, Y. Shen, F. M. Wang and X. B. Zhang, Constructing hierarchical mushroom-like bifunctional NiCo/$NiCo_2S_4$@NiCo/Ni foam electrocatalysts for efficient overall water splitting in alkaline media, *Electrochim. Acta*, 2018, **265**, 19–31, DOI: 10.1016/j.electacta.2018.01.150.

12 F. Zakeri, A. Javid, Y. Orooji, A. Fazli, A. Khataee and A. Khataee, Al-Ce co-doped $BaTiO_3$ nanofibers as a high-performance bifunctional electrochemical supercapacitor and water-splitting electrocatalyst, *Sci. Rep.*, 2024, **14**, 9833, DOI: 10.1016/j.jece.2025.119553.

13 X. Wang, B. Zhang, J. Zhang, X. Jiang, K. Liu, H. Wang, X. Yuan, H. Xu, Y. Zheng, G. Ma and C. Zhong, Conformal and conductive biofilm-bridged artificial Z-scheme system for visible light-driven overall water splitting, *Sci. Adv.*, 2024, **10**, eadn6211, DOI: 10.1126/sciadv.adn6211.

14 B. M. Thamer, M. M. A. Hameed and A. M. Al Enizi, Fabrication of highly dispersed bimetallic Ni-Mo@CNFs by sol-gel assisted electrospinning for methanol oxidation electrocatalysis, *J. Alloys Compd.*, 2023, **952**, 169956, DOI: 10.1016/j.jallcom.2023.169956.

15 X. Zheng, Y. Cao, H. Wang, J. Zhang, M. Zhao, Z. Huang, Y. Wang, L. Zhang, Y. Deng, W. Hu and X. Han, Designing Breathing Air-electrode and Enhancing the Oxygen Electrocatalysis by Thermoelectric Effect for Efficient Zn-air Batteries, *Angew. Chem., Int. Ed.*, 2023, **62**, e202302689, DOI: 10.1002/anie.202302689.

16 S. Chandrasekaran, P. Zhang, F. Peng, C. Bowen, J. Huo and L. Deng, Tailoring the geometric and electronic structure of tungsten oxide with manganese or vanadium doping toward highly efficient electrochemical and photoelectrochemical water splitting, *J. Mater. Chem. A*, 2019, **7**, 6161–6172, DOI: 10.1039/c8ta12238e.

17 R. Rajalakshmi, A. Rebekah, C. Viswanathan and N. Ponpandian, Evolution of intrinsic 1-3D WO_3 nanostructures: Tailoring their phase structure and morphology for robust hydrogen evolution reaction, *Chem. Eng. J.*, 2022, **428**, 132013, DOI: 10.1016/j.cej.2021.132013.

18 J. Yang, X. Chen, X. Liu, Y. Cao, J. Huang, Y. Li and F. Liu, From Hexagonal to Monoclinic: Engineering Crystalline Phase to Boost the Intrinsic Catalytic Activity of Tungsten Oxides for the Hydrogen Evolution Reaction, *ACS Sustainable Chem. Eng.*, 2021, **9**, 5642–5650, DOI: 10.1021/acssuschemeng.1c00485.

19 H. Huang, L. Xu, D. Yoon Woo, S. Kim, S. Min Kim, Y. Kyeong Kim, J. Byeon and J. Lee, Refining the surface properties of $WO_{2.7}$ by vacancy engineering and transition metals doping for enhanced alkaline hydrogen evolution reaction, *Chem. Eng. J.*, 2023, **451**, 138939, DOI: 10.1016/j.cej.2022.138939.

20 Y. Long, P. Jiang, P. Liao, C. Yang, S. Li, J. Xian, Y. Sun, Q. Liu and G. Li, Electronic Structure Regulation by Fe Doped Ni-Phosphides for Long-term Overall Water Splitting at Large Current Density, *Small*, 2024, **20**, 2403991, DOI: 10.1002/smll.202403991.

21 D. Wang, H. Li, N. Du and W. Hou, Single Platinum Atoms Immobilized on Monolayer Tungsten Trioxide Nanosheets as an Efficient Electrocatalyst for Hydrogen Evolution Reaction, *Adv. Funct. Mater.*, 2021, **31**, 2009770, DOI: 10.1002/adfm.202009770.

22 H. Chen, J. Yu, L. Liu, R.-T. Gao, Z. Gao, Y. Yang, Z. Chen, S. Zhan, X. Liu, X. Zhang, H. Dong, L. Wu and L. Wang, Modulating Pt-N/O Bonds on Co-doped WO_3 for Acid Electrocatalytic Hydrogen Evolution with Over 2000 h Operation, *Adv. Energy Mater.*, 2024, **14**, 2303635, DOI: 10.1002/aenm.202303635.

23 X. Jiang, H. Jang, S. Liu, Z. Li, M. G. Kim, C. Li, Q. Qin, X. Liu and J. Cho, The Heterostructure of Ru_2P/WO_3/NPC Synergistically Promotes H_2O Dissociation for Improved Hydrogen Evolution, *Angew. Chem., Int. Ed.*, 2021, **60**, 4110–4116, DOI: 10.1002/anie.202014411.

24 X. Zheng, X. Shi, H. Ning, R. Yang, B. Lu, Q. Luo, S. Mao, L. Xi and Y. Wang, Tailoring a local acid-like microenvironment for efficient neutral hydrogen evolution, *Nat. Commun.*, 2023, **14**, 4209, DOI: 10.1038/s41467-023-39963-8.

25 W. Liang, M. Zhou, X. Lin, J. Xu, P. Dong, Z. Le, M. Yang, J. Chen, F. Xie, N. Wang, Y. Jin and H. Meng, Nickel-doped tungsten oxide promotes stable and efficient hydrogen evolution in seawater, *Appl. Catal., B*, 2023, **325**, 122397, DOI: 10.1016/j.apcatb.2023.122397.

26 F. Li, M. Jiang, C. Lai, H. Xu, K. Zhang and Z. Jin, Yttrium- and Cerium-Codoped Ultrathin Metal-Organic Framework Nanosheet Arrays for High-Efficiency Electrocatalytic Overall Water Splitting, *Nano Lett.*, 2022, **22**, 7238–7245, DOI: 10.1021/acs.nanolett.2c02755.

27 K. K. Mandari, Y. Im, Y.-A. Lee and M. Kang, Highly efficient 2D/2D NiCo-LDH/$CuInS_2$ nanocomposites for electrocatalytic hydrogen and oxygen evolution reactions, *Fuel*, 2025, **388**, 134505, DOI: 10.1016/j.fuel.2025.134505.

28 W. Liu, J. Bao, M. Guan, Y. Zhao, J. Lian, J. Qiu, L. Xu, Y. Huang, J. Qian and H. Li, Nickel-cobalt-layered double hydroxide nanosheet arrays on Ni foam as a bifunctional electrocatalyst for overall water splitting, *Dalton Trans.*, 2017, **46**, 8372–8376, DOI: 10.1016/j.jpowsour.2014.12.085.

29 R. Subbaraman, D. Tripkovic, D. Strmcnik, K.-C. Chang, M. Uchimura, A. P. Paulikas, V. Stamenkovic and N. M. Markovic, Enhancing Hydrogen Evolution Activity in Water Splitting by Tailoring Li^+-$Ni(OH)_2$-Pt Interfaces, *Science*, 2011, **334**, 1256–1260, DOI: 10.1126/science.1211934.

30 B. Sun, S. Lou, W. Zheng, Z. Qian, C. Cui, P. Zuo, C. Du, J. Xie, J. Wang and G. Yin, Synergistic engineering of defects and architecture in Co_3O_4@C nanosheets toward Li/Na ion batteries with enhanced pseudocapacitances, *Nano Energy*, 2020, **78**, 105366, DOI: 10.1016/j.nanoen.2020.105366.

31 Z. W. Seh, J. Kibsgaard, C. F. Dickens, I. Chorkendorff, J. K. Nørskov and T. F. Jaramillo, Combining theory and experiment in electrocatalysis: Insights into materials design, *Science*, 2017, **355**, eaad4998, DOI: 10.1016/j.coelec.2019.03.009.

32 C. Jiao, M. Hassan, X. Bo and M. Zhou, $Co_{0.5}Ni_{0.5}P$ nanoparticles embedded in carbon layers for efficient electrochemical water splitting, *J. Alloys Compd.*, 2018, **764**, 88–95, DOI: 10.1016/j.jallcom.2018.06.008.

33 X. Jiao, Z. Chen, X. Li, Y. Sun, S. Gao, W. Yan, C. Wang, Q. Zhang, Y. Lin, Y. Luo and Y. Xie, Defect-Mediated Electron-Hole Separation in One-Unit-Cell $ZnIn_2S_4$ Layers for Boosted Solar-Driven CO_2 Reduction, *J. Am. Chem. Soc.*, 2017, **139**, 7586–7594, DOI: 10.1021/jacs.7b02290.

34 H. Jiang, H. Qin, P. Zhou, L. Kong, C. Wang, Z. Ji, X. Shen, G. Zhu and A. Yuan, Partial sulfidation strategy to NiCo-LDH@NiCoS coupled with NiFe-LDH for highly efficient overall water splitting, *Int. J. Hydrogen Energy*, 2024, **58**, 892–901, DOI: 10.1016/j.ijhydene.2024.01.292.

35 S. Zhao, H. Gao, Y. Guo, Q. Zhang and X. Zhao, Facile synthesis of Ce-doped WSe_2 nanoflowers on Ni foam for improved hydrogen evolution reaction, *Mol. Catal.*, 2025, **583**, 115213, DOI: 10.1016/j.mcat.2025.115213.

36 C. Mao, Z. Shi, J. Peng, L. Ou, Y. Chen and J. Huang, Hierarchically Porous Carbonized Wood Decorated with $MoNi_4$-Embedded MoO_2 Nanosheets: An Efficient Electrocatalyst for Water Splitting, *Adv. Funct. Mater.*, 2024, **34**, 2308337, DOI: 10.1002/adfm.202308337.

37 W. Li, Y. Chen, S. Liu and J. Tang, Enhanced electrocatalytic performance of carbon-coated $NiCoO_2$/NiCo composites for efficient water splitting, *Sci. Rep.*, 2025, **15**, 12294, DOI: 10.1038/s41598-025-96880-0.

38 C. C. Hao, R. Zhang, W. Z. Wang, Y. J. Liang, J. L. Fu, B. Zou and H. L. Shi, Efficient charge transfer and separation of TiO_2@NiCo-LDH core-shell nanowire arrays for enhanced photoelectrochemical water-splitting, *J. Solid State Electrochem.*, 2019, **23**, 2343–2353, DOI: 10.1007/s10008-019-04304-7.

39 M. Elrouby, H. M. A. El-Lateef and M. Sadek, Electrodeposited Pt nanorods on a novel flowered-like nanostructured Ni-Co alloy as an electrocatalyst for methanol oxidation, *Int. J. Hydrogen Energy*, 2019, **44**, 13820–13834, DOI: 10.1016/j.ijhydene.2019.03.261.

40 F. O. Boakye, K. Harrath, D. Zhang, Y. You, W. Zhang, Z. Wang, H. Zhang, J. Zhu, J. Long, J. Zhu, G. Yasin, K. A. Owusu, M. Tabish, L. Zhang, D. Wang, X. Shi, Z. Jiang, B. Wu, L. Mai and W. Zhao, Synergistic Engineering of Dopant and Support of Ru Oxide Catalyst Enables Ultrahigh Performance for Acidic Oxygen Evolution, *Adv. Funct. Mater.*, 2024, **34**, 2408714, DOI: 10.1002/adfm.202408714.

41 M. Li, J. Yang, S. Li, L. Deng, S. Zhao, L. Li, S. F. Hung, G. Xing, T. Wang, Y. Liang, J. Ren, Y. Wu and S. Peng, Rare-Earth-Induced Intermediate-Spin Co Centers in $MnCo_2O_{4.5}$ for Sustainable Acidic Water Oxidation, *J. Am. Chem. Soc.*, 2025, **147**, 45680–45690, DOI: 10.1021/jacs.5c17361.

42 J. Yu, H. V. Demir and M. Sharma, Optical signatures of lattice strain in chemically doped colloidal quantum wells, *Nat. Commun.*, 2025, **16**, 823, DOI: 10.1038/s41467-025-55984-x.

43 M. Zhang, H. Xu, H. Yang, X. Shang, M. Yuan, Y. Fu, Y. Xiao, S. Wang, X. Wang, B. Jia, S. Li and T. Ma, Electronic Modulation of Nickel Cobalt Phosphide Nanosheets by Ce

Doping for Efficient Overall Water Splitting, *Small*, 2025, **21**, 2504837, DOI: 10.1002/smll.202504837.

44 H. N. Dhandapani, D. Mahendiran, A. Karmakar, P. Devi, S. Nagappan, R. Madhu, K. Bera, P. Murugan, B. R. Babu and S. Kundu, Boosting of overall water splitting activity by regulating the electron distribution over the active sites of Ce doped NiCo-LDH and atomic level understanding of the catalyst by DFT study, *J. Mater. Chem. A*, 2022, **10**, 17488–17500, DOI: 10.1039/d2ta04647d.

45 Y. Liu, M. Ding, Y. Qin, B. Zhang, Y. Zhang and J. Huang, Crystalline/Amorphous Mo-$Ni(OH)_2/Fe_xNi_y(OH)_{3x+2y}$ hierarchical nanotubes as efficient electrocatalyst for overall water splitting, *J. Colloid Interface Sci.*, 2024, **657**, 219–228, DOI: 10.1016/j.jcis.2023.11.151.

46 Y. Hu and C. Wang, Electrodeposition of nickel-cobalt alloys from metal chloride-L-serine deep eutectic solvent for the hydrogen evolution reaction, *J. Mater. Chem. A*, 2024, **12**, 16769–16779, DOI: 10.1039/d4ta02433h.

47 Y. Yang, X. Li, G. Liu, H. Liu, Y. Shi, C. Ye, Z. Fang, M. Ye and J. Shen, Hierarchical Ohmic Contact Interface Engineering for Efficient Hydrazine-Assisted Hydrogen Evolution Reaction, *Adv. Mater.*, 2024, **36**, 2307979, DOI: 10.1002/adma.202307979.

48 M. Hu, Y. Qian, R. Zhang, C. Guo, L. Yang and L. Li, Interfacial electronic modulation of NiCo decorated nano-flowered MoS_2 on carbonized wood as a remarkable bifunctional electrocatalyst for boosting overall water splitting, *J. Colloid Interface Sci.*, 2025, **677**, 729–738, DOI: 10.1016/j.jcis.202407209.

49 Y. Shen, Y. Dou, L. Sun, L. Huo and H. Zhao, Work Function-Induced Electronic Modulation in NiCo Alloy for Electrochemical Nitrate Reduction, *Inorg. Chem.*, 2025, **64**, 7052–7063, DOI: 10.1021/acs.inorgchem.5c00362.

50 Q. Wen, J. Duan, W. Wang, D. Huang, Y. Liu, Y. Shi, J. Fang, A. Nie, H. Li and T. Zhai, Engineering a Local Free Water Enriched Microenvironment for Surpassing Platinum Hydrogen Evolution Activity, *Angew. Chem., Int. Ed.*, 2022, **61**, 202206077, DOI: 10.1002/anie.202206077.

51 C. Liu, Y. Han, L. Yao, L. Liang, J. He, Q. Hao, J. Zhang, Y. Li and H. Liu, Engineering Bimetallic NiFe-Based Hydroxides/Selenides Heterostructure Nanosheet Arrays for Highly-Efficient Oxygen Evolution Reaction, *Small*, 2021, **17**, 2007334, DOI: 10.1002/smll.202007334.

52 B. Luo, Y.-Z. Wang, D. Li, H. Shen, L.-X. Xu, Z. Fang, Z. Xia, J. Ren, W. Shi and Y.-C. Yong, A Periplasmic Photosensitized Biohybrid System for Solar Hydrogen Production, *Adv. Energy Mater.*, 2021, **11**, 2100256, DOI: 10.1002/aenm.202100256.

53 G. Barati Darband, D. Iravani, M. Zhang, M. Maleki, S. Huang, S. M. Khoshfetrat, R. Andaveh and J. Li, Sustainable and energy-saving hydrogen production via binder-free and in situ electrodeposited Ni–Mn–S nanowires on Ni–Cu 3-D substrates, *Nanoscale*, 2025, **17**, 2162–2173, DOI: 10.1039/D4NR03486D.

54 A. Talebi and G. Barati Darband, Ultra-fast one-step electrochemical synthesize of Ni-Mn-P as an active and stable electrocatalyst for green hydrogen production, *Fuel*, 2025, **397**, 135427, DOI: 10.1016/j.fuel.2025.135427.

55 R. Abedi and G. Barati Darband, Interfacial surface engineering of Co-Mn-P ultrathin nanosheets on Ni-Co hierarchical nanostructure for boosting electrochemical active sites in overall water splitting, *J. Power Sources*, 2025, **641**, 236840, DOI: 10.1016/j.jpowsour.2025.236840.

56 S. Khademjafari, A. Sabour Rouhaghdam, D. Iravani, A. Talebi, G. Barati Darband and S. Shanmugam, Binder-free Co-P@Ni-Cu cedar leaf-like hierarchical structure as an efficient and stable electrocatalyst for hydrogen and oxygen evolution reactions, *J. Power Sources*, 2026, **661**, 238608, DOI: 10.1016/j.jpowsour.2025.238608.

57 Y. Li, W. Zhou, Z. Huang, Q. Pan, X. Zhao, M. Zhang, X. Hao, D. Li and J. Xu, Flexible Ce-doped WO_3 nanowire arrays with enriched oxygen vacancies for soft-packaged asymmetric supercapacitor, *Appl. Surf. Sci.*, 2024, **655**, 159616, DOI: 10.1016/j.apsusc.2024.159616.